CHINESE OPTICS LETTERS

Vol. 22, No. 4 | April 2024

Active metasurface via magnetic control for tri-channel polarization multiplexing holography

Yu Bi (毕 钰)[1*], Lingling Huang (黄玲玲)[2**], Tuo Li (李 拓)[1], Changhong Wang (王长红)[1], Xiaofeng Zou (邹晓峰)[1], Lang Zhou (周 朗)[1], and Guoguo Kang (康果果)[2]

[1] Shandong Inspur Artificial Intelligence Research Institute Company Limited, Jinan 250013, China

[2] MIIT Key Laboratory of Photonics Information Technology, School of Optics and Photonics, Beijing Institute of Technology, Beijing 100081, China

*Corresponding author: biyu01@inspur.com

**Corresponding author: huanglingling@bit.edu.cn

Received October 25, 2023 | Accepted December 13, 2023 | Posted Online April 18, 2024

Active metasurfaces have recently attracted more attention since they can make the light manipulation be versatile and real-time. Metasurfaces-based holography possesses the advantages of high spatial resolution and enormous information capacity for applications in optical displays and encryption. In this work, a tunable polarization multiplexing holographic metasurface controlled by an external magnetic field is proposed. The elaborately designed nanoantennas are arranged on the magneto-optical intermediate layer, which is placed on the metallic reflecting layer. Since the non-diagonal elements of the dielectric tensor of the magneto-optical material become non-zero values once the external magnetic field is applied, the differential absorption for the left and right circularly polarized light can be generated. Meanwhile, the amplitude and phase can be flexibly modulated by changing the sizes of the nanoantennas. Based on this, the dynamic multichannel holographic display of metasurface in the linear and circular polarization channels is realized via magnetic control, and it can provide enhanced security for optical information storage. This work paves the way for the realization of magnetically controllable phase modulation, which is promising in dynamic wavefront control and optical information encryption.

Keywords: active metasurface; magneto-optical effect; polarization multiplexing holography; dynamic holographic display.
DOI: 10.3788/COL202422.043601

1. Introduction

Light manipulation via nanostructured materials plays a significant role in modern nanophotonics. Specially, combining the functional materials with engineered structures provides an exceptional route for exploring new principles and expansive applications for dynamic light manipulation. For example, tunable metasurfaces are widely used in zoom lens[1,2], beam generation[3,4], optical switches[5,6], and dynamic holographic displays[7–9] via incorporating a functional material into the nanostructured design. The optical properties can be affected by different external excitations, such as electrical[10], optical[11], thermal[12], mechanical[13], and magnetic[14] stimulation. Notably, the active metasurface via magnetic control has the advantages of sub-nanosecond ultrafast response and is non-invasive, which exhibits an important potential in dynamic light manipulation.

The magneto-optical (MO) metasurface can provide multiple degrees of freedom for light control via magneto-optical effects, such as the Faraday effect[15–17] and Kerr effect[18,19]. This feature makes it widely applied in various fields such as modulator[20,21], isolator[22–24], chiral sensing[25,26], biochemical sensing[27,28], magnetic field sensing[29–31], and MO switch[32,33]. However, in terms of the MO modulation, it is challenging to make the nanostructure achieve a strong MO response due to the weak effect of the MO material. Therefore, most studies emphasize using magneto-plasmonic or dielectric resonance to improve the modulation efficiency of the amplitude and polarization rotation of the MO metasurface[34–38]. Nevertheless, a few studies have focused on the phase modulation of MO metasurfaces by flexibly designing the nanostructure. Although it has been proved that an MO metasurface can realize superchiral light field manipulation and dynamic wavefront control by elaborately arranging the nanoantennas, they are mainly applicable in the terahertz regime, and less attention has been paid to the applications of the MO metasurface in the optical regime and holographic display[39,40]. Therefore, flexibly designing the meta-atoms to achieve the information encoding function in the optical regime should be studied extensively. In the previous work, we reported the method for realizing the magnetically controllable holographic encryption based on an MO metasurface. Nevertheless, it can

only realize a dynamic holographic display in two linearly polarized channels via magnetic control and does not delve into the resonance behavior of the structure[41].

Here, we investigate the complex amplitude modulation and resonance properties of a tunable MO metasurface, which comprises elaborately designed metallic nanoantennas arranging on the MO intermediate layer and the metallic reflecting layer. Particularly, we demonstrate that the identical MO metasurface can realize switchable tri-channel polarization multiplexing holography by using magnetic control and suitable nanoantenna arrangements. When an external magnetic field is applied or not, the three different holographic images are reconstructed in the E_{xx} linear polarization channel and the E_{ll} and E_{rl} circular polarization channels. The switchable reconstructed images, such as the pattern "flower" (in the E_{xx} channel), the Chinese character "中" (in the E_{ll} channel), and the pattern "butterfly" (in the E_{rl} channel), can be observed in the Fourier plane using the finite-difference time-domain (FDTD) and the modified Gerchberg–Saxton (GS) holographic algorithm. This work will pave the way for the application of dynamic multichannel metasurface holographic display via magnetic control, which is significant in optical information encryption.

2. Model Setup

As is shown in Fig. 1, the proposed MO metasurface consists of a tri-layer structure deposited on a glass substrate. Specifically, the delicately designed metallic (Au) nanoantennas are arranged on the MO intermediate layer, which is placed on the metallic (TiN) reflecting layer. This configuration is chosen because the resonator cavity formed by the double-layer metals can improve

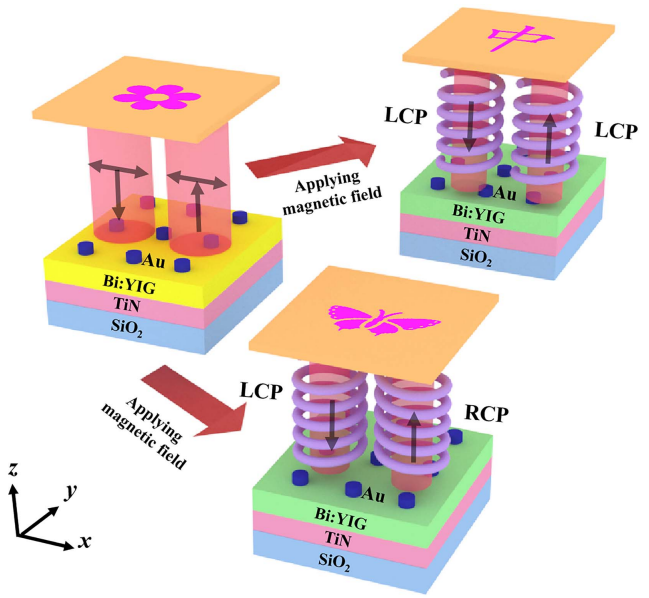

Fig. 1. Schematic of the magnetically controllable multichannel holographic display based on the MO metasurface.

the MO response and polarization conversion efficiency. In this structure, we chose bismuth-substituted yttrium iron garnet (Bi:YIG) as the MO layer due to its high MO coefficient in the optical regime. Since the applied magnetic field is along the z-axis, which makes the magnetization of the Bi:YIG film perpendicular to the sample and parallel to the incident plane (x–z plane), the off-diagonal elements ε_{xy} and ε_{yx} of its dielectric tensor become non-zero components, and the dielectric tensor of the MO material can be described as follows:

$$\begin{pmatrix} \varepsilon_{xx} & \varepsilon_{xy} & 0 \\ -\varepsilon_{xy} & \varepsilon_{yy} & 0 \\ 0 & 0 & \varepsilon_{zz} \end{pmatrix}, \tag{1}$$

where $\varepsilon_{xy} = -ig$, and g describes the magnetization-induced gyration of the Bi:YIG film. Here, we assume that the Bi:YIG film is optically isotropic, and its second-order MO effect is negligible. Since the dielectric tensor of the Bi:YIG film is slightly dispersive over the designing wavelength range, the average value of the tensor with $\varepsilon_{xx} = \varepsilon_{yy} = \varepsilon_{zz} = 5.5 + i0.0025$ and $g = (1 - i0.15) \times 10^{-2}$ is adopted[42,43]. When there is no external magnetic field, the off-diagonal elements turn into zero, which means the Bi:YIG film will not produce the MO effect. Additionally, the frequency-dependent permittivity of the gold is characterized by the well-known Drude model, which is given by Ref. [44] and can be expressed as

$$\varepsilon = \varepsilon_\infty - \frac{\omega_p^2}{\omega^2 + i\gamma\omega}, \tag{2}$$

where $\varepsilon_\infty = 7.9$, $\omega_p = 8.77$ eV, and $\gamma = 1.13 \times 10^{14}$ s^{-1} is set to fit the empirical data over the designing wavelength range. The dielectric function of the TiN is provided by Palik in the material database of the FDTD, and the permittivity of glass is set to 2.13.

To characterize the reflection of the MO metasurface, we build the model using FDTD. Initially, we set the height of the Au nanoantennas to 50 nm and the thicknesses of the TiN reflecting layer to 200 nm, respectively. The intermediate layer is a continuous Bi:YIG film with a thickness of 400 nm, and the lattice is identical in the x- and y-directions, i.e., $P_x = P_y = P$. Here, we set the period of the lattice to 600 nm, and we set the periodic boundary conditions in the x- and y-directions while the perfectly matched layer boundary condition is set in the z-direction. Moreover, the mesh sizes in the x-, y-, and z-directions are set as 20 nm, 20 nm, and 5 nm, respectively. Normally, the incident linearly x-polarized plane wave or circularly polarized light is used to excite the structure, and the latter is formed by the superposition of two linearly polarized lights with a polarization angle and phase difference of 90°. The phase is set as 90° or −90° to distinguish the left or right circularly polarized (LCP or RCP) light. When the TM-polarized (x-polarized) light is illuminated, the reflectance spectrum of the structure is calculated, as shown in Fig. 2. It can be seen that the maximum reflectance is approximately 0.8, and

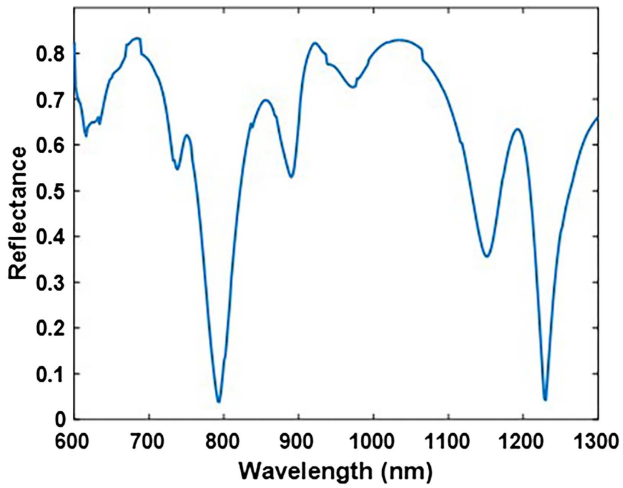

Fig. 2. Reflectance spectrum of the MO metasurface with the TM-polarized incident light.

there are two resonant dips in the reflectance spectra. The decrease in the diffraction efficiency is mainly originated from the loss of the metal materials. The generated plasmon resonance mode at the interface of the metal/dielectric layer and the waveguide mode inside the MO layer make for strong electromagnetic field enhancement and further exhibit asymmetric Fano resonance in the reflectance spectra.

Additionally, to delve into the physics of the observed resonance modes, we take a deeper look into the resonant behavior of the hybrid MO metasurface. The spatial distributions of the electric and magnetic fields at the resonant wavelength 922 nm are demonstrated in Fig. 3. The field distributions clearly reveal that a TM waveguide-plasmon hybrid mode is excited. On the one hand, the TM-polarized light drives a collective oscillation of electrons in the metallic nanoantenna and excites a particle plasmon resonance, which enhances the near field. On the other hand, the periodically arranged nanoantennas make the light scatter into the MO waveguide layer and excite a TM-guided mode. Additionally, the double-layer metals form the resonator cavity, which can enhance the reflected light.

3. Design of the MO Metasurface

To acquire the complex amplitude modulation of the MO metasurface, we conduct a structural parameter sweep to the periodic nanoantenna unit. The length and width of the nanoantenna are varied from 100 to 500 nm with an interval of 10 nm. Figure 4 shows the complex amplitude modulation of the structure in the linearly and circularly polarized channels when the external magnetic field is applied. Specifically, Figs. 4(a)–4(d) show the amplitude and phase modulation of the co- and cross-polarized reflected light with the x-polarized incident light, while Figs. 4(e)–4(g) show the amplitude and phase modulation of the LCP and the RCP reflected light with the LCP incident light. It should be noted that in the absence of an external magnetic field, there exists no y-polarized reflected light when the x-polarized light is incident, which indicates that the reflected light in the magnetized MO layer has undergone a polarization rotation. However, the diffraction efficiency of the y-polarized reflected light with the applied magnetic field only reaches up to 0.02, which means it is not suitable for reconstructing the holograms. Moreover, there exists a considerable difference of the complex amplitude modulation in the linearly and circularly polarized channels. The diffraction efficiency in the E_{xx} channel covers from 0.19 to 0.88. Also, the diffraction efficiencies in the E_{ll} and E_{rl} channels cover from 0.37 to 0.75 and 0.53 to 0.91, respectively. It can be seen that the amplitude modulations vary widely while the phase modulations vary slightly. Therefore, to realize switchable multichannel holographic display via magnetic control, it is necessary to select the desired structures to encode the binary amplitude-only holograms. Remarkably, the black circles in the sub-diagram of Fig. 4 represent the amplitudes and phases of the selected nanoantenna structures in different polarization channels.

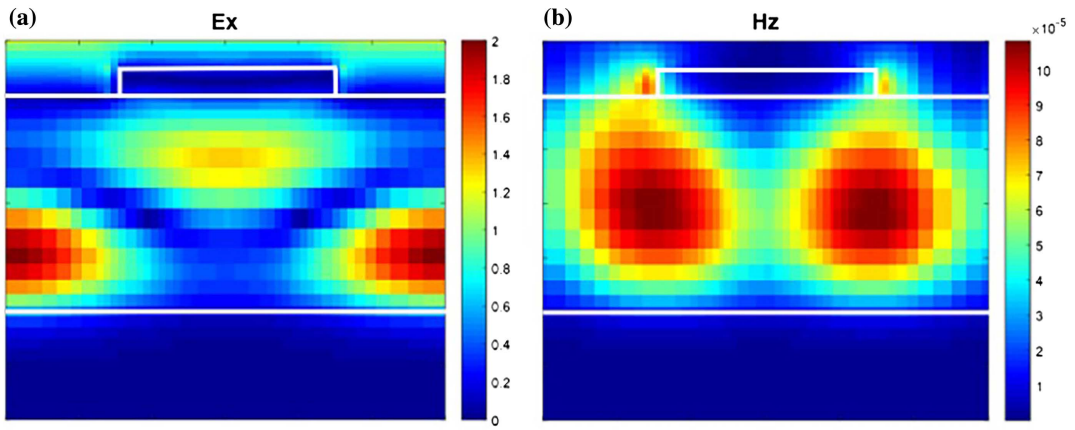

Fig. 3. Calculated spatial distribution of (a) the electric and (b) the magnetic field for normally incident TM-polarized light. White lines denote the cross section of the structure.

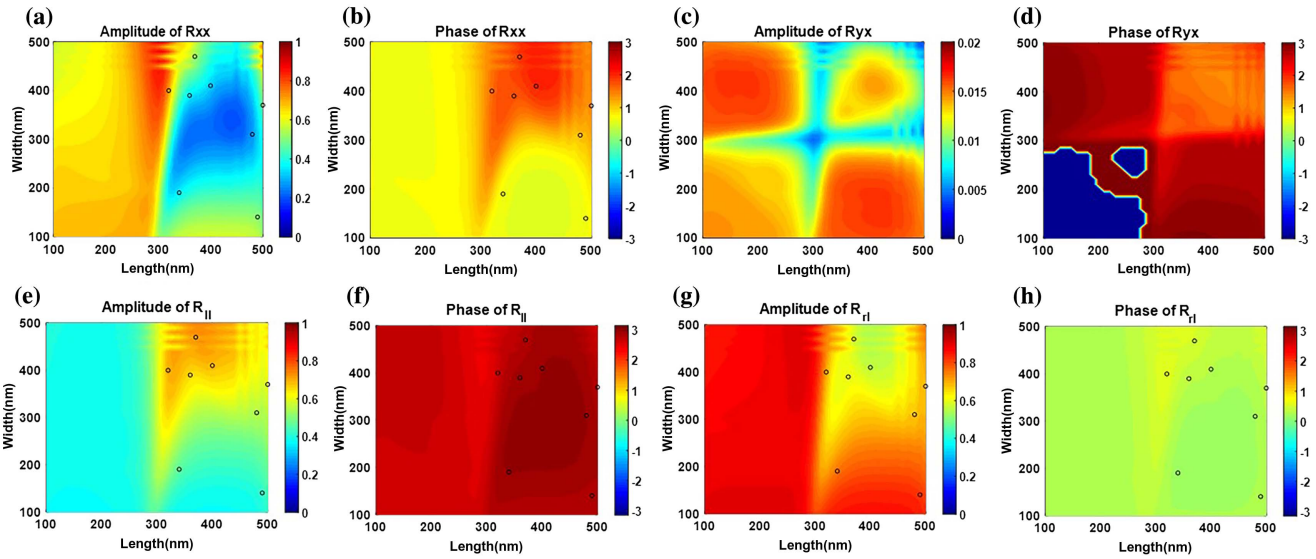

Fig. 4. Complex amplitude modulation in the linear and circular polarization channels with the applied magnetic field. (a)–(d) Amplitude and phase modulation of the co- and cross-polarized reflected light with the *x*-polarized incident light. (e)–(h) Amplitude and phase modulation of the LCP and RCP reflected light with the LCP incident light.

As is known, the hologram of each polarization channel is encoded by a 2-bit amplitude, and each bit amplitude corresponds to a nanoantenna structure. Therefore, to encode independent binary-amplitude holograms in the three switchable polarization channels, eight (2^3) nanoantenna structures need to be selected. The phase modulations of the selected nanostructures in each polarization channel are required to be as uniform as possible, and the amplitude modulations are required to be as large a proportion of high amplitude to low amplitude as possible. Specifically, the amplitude combinations of the selected structures in both switchable polarization channels (in the E_{xx} and E_{ll} channels or in the E_{xx} and E_{rl} channels) need to satisfy (0, 0), (0, 1), (1, 0), and (1, 1), in which 0 and 1 represent only the low and high amplitude types, not the actual modulation efficiency. Meanwhile, this principle should also apply to the E_{ll} and E_{rl} channels. The selected geometric parameters are shown in Table 1, and the complex amplitudes of the selected structures in the three polarization channels are shown in Fig. 5. It is obvious that the phase fluctuation of most of the structures is slight in a specific polarized channel, which contributes to the noise reduction of the generated holograms. Moreover, the amplitude combinations of the selected structures in the E_{xx} and E_{ll} channels, the E_{xx} and E_{rl} channels, or the E_{ll} and E_{rl} channels all satisfy (0, 0), (0, 1), (1, 0), and (1, 1). Notably, the amplitudes of the selected structures are not absolute 0 or 1, only that there is a relatively large difference between high and low amplitudes. Although the amplitude modulation in individual polarization channels does not satisfy absolutely uniform high and low amplitudes, since it is a binary-amplitude hologram, the uneven amplitude values can be regarded as multiplied by a constant, which will only affect the overall

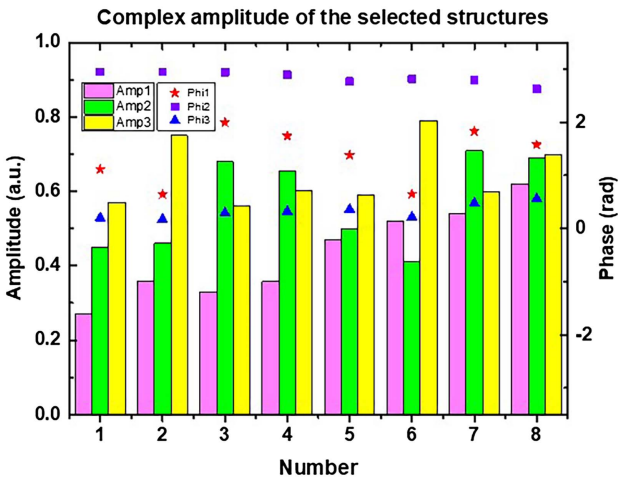

Fig. 5. Complex amplitudes of the selected structures in the E_{xx}, E_{ll}, and E_{rl} channels. The left axis demonstrates the amplitude distribution of the reflection light, with the pink/green/yellow bars representing the amplitude distribution in the E_{xx}, E_{ll}, and E_{rl} channels, respectively. The right axis depicts the phase distribution of the reflection light, with the star/triangle/square representing the phase distribution in the E_{xx}, E_{ll}, and E_{rl} channels, respectively.

Table 1. Geometric Parameters of the Selected Structures.

	Number							
Parameter	1	2	3	4	5	6	7	8
Length (nm)	480	340	400	360	500	490	370	320
Width (nm)	310	190	410	390	370	140	470	400

efficiency of the reconstructed hologram but will not affect the imaging quality. Also, although the individual phase values are biased, this does not affect the reconstruction of the holographic image due to its tolerance to the phase noise.

4. Implementation of the Multichannel Holographic Display

Furthermore, we use the modified GS algorithm and FDTD to reconstruct the switchable holographic images in the Fourier plane of the MO metasurface. The encoding scheme of the multiple binary-amplitude holograms within one identical MO metasurface and the design principle of the nanoantenna arrangement are illustrated in Fig. 6. Suppose that the MO metasurface is made up of many pixel units, and the selected structures are respectively arranged in each unit. The amplitude modulation of one identical structure in different polarization channels might be 0 or 1. The amplitude combinations of the selected structures should satisfy the three-bits amplitude modulation (0, 0, 0), (0, 0, 1), (0, 1, 0), (0, 1, 1) (1, 0, 1), (1, 0, 0), (1, 1, 0), and (1, 1, 1) in the E_{xx}, E_{ll}, and E_{rl} channels, respectively. Consequently, the independent holographic images can be reconstructed between each polarization channel.

First, we generate the multiple binary-amplitude holograms using the modified GS algorithm. Considering the required capacity for the calculation, we make images of 100 × 100 pixels. Based on the complex amplitude of the selected structure, the multiple iterative loops of inverse fast Fourier transform (FFT) are performed between the hologram and reconstructed image. Afterwards, the optimal complex amplitude holograms can be generated based on the binary-amplitude hologram algorithm. The three reconstructed hologram images in the different polarization channels are calculated by the GS algorithm, as shown in Figs. 7(a)–7(c). Then, we encode the three holograms into one identical MO metasurface according to the coding method illustrated in Fig. 6, and the designed MO metasurface array is further modeled using the FDTD method. Since the unit period of the structure is 600 nm, the size of the modeled MO metasurface is 60 μm × 60 μm, and the far-field reconstructed images in the Fourier plane are simulated as shown in Figs. 7(d)–7(f).

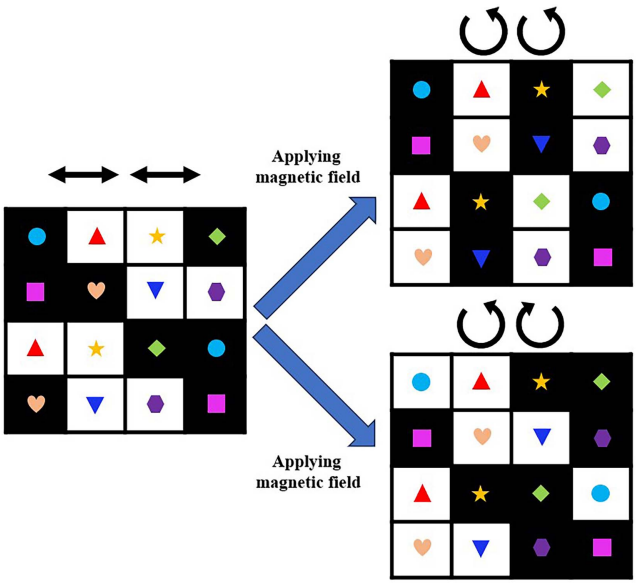

Fig. 6. Schematic illustration of encoding multiple binary-amplitude holograms within one identical MO metasurface. The box represents each pixel unit. The boxes with different shaped markers represent the selected eight structures. The black and white boxes represent the amplitude modulation of 0 and 1 for the selected structure in different polarization channels. The black arrows indicate the input/output linearly and circularly polarized light.

Similarly, we can successfully observe the reconstructed images of the structure in different polarization channels. The pattern "flower" is reconstructed in the E_{xx} polarization channels at the state of the applied magnetic field, while the Chinese character "中" and the pattern "butterfly" are reconstructed in the E_{ll} and E_{rl} polarization channels without the applied magnetic field. The results are comparable with the ones based on the GS algorithm, and there is almost no crosstalk between each polarization channel. Since the reconstructed images are based on the binary-amplitude holographic algorithm, there exists conjugate images. Also, we can note that the reconstructed image quality using the full-wave simulation is deteriorated a bit compared to the ones using the GS algorithm. On the one hand, the image pixel count and the meshing accuracy are limited given the capacity required for the calculation. On the other hand, the near-field coupling between the adjacent nanoantenna will affect the image quality. Nevertheless, due to the strong robustness and relative larger tolerance of the amplitude noises of the binary amplitude-only hologram, we can still get the reconstructed image prototype to verify the switchable multichannel holographic display function of the MO metasurface.

Here, we propose the method for fabricating the device and building the experimental setup. In terms of device fabrication, the metallic TiN film of 200 nm on the silica substrate can be first deposited by pulsed laser deposition (PLD) equipped with a KrF excimer laser. Then, the MO film can be deposited by PLD or by the magnetron sputtering process, of which PLD is the better method since it may take several hours to deposit the Bi:YIG film with a thickness of 400 nm by magnetron sputtering. After deposition, the Bi:YIG film should undergo the high-temperature annealing process to make it crystallized. The TiN film can support the high-temperature atmosphere. Subsequently, gold nanoantennas can be fabricated by sputtering, electron beam lithography, and lift-off process, respectively. As for the experimental setup, a light source illuminates the sample after passing through the polarizers, lens, and beam splitter. Therein, a pair of linear polarizers or a combination of linear polarizers and quarter-wave plates is placed ahead and behind the sample to obtain the desired incident or reflective linearly/circularly polarized beam. Meanwhile, the MO metasurface sample is placed in the focal plane of an objective lens and a set of perforated permanent magnets. The permanent magnet produces a fixed magnetic field, which is perpendicular to the sample surface, to

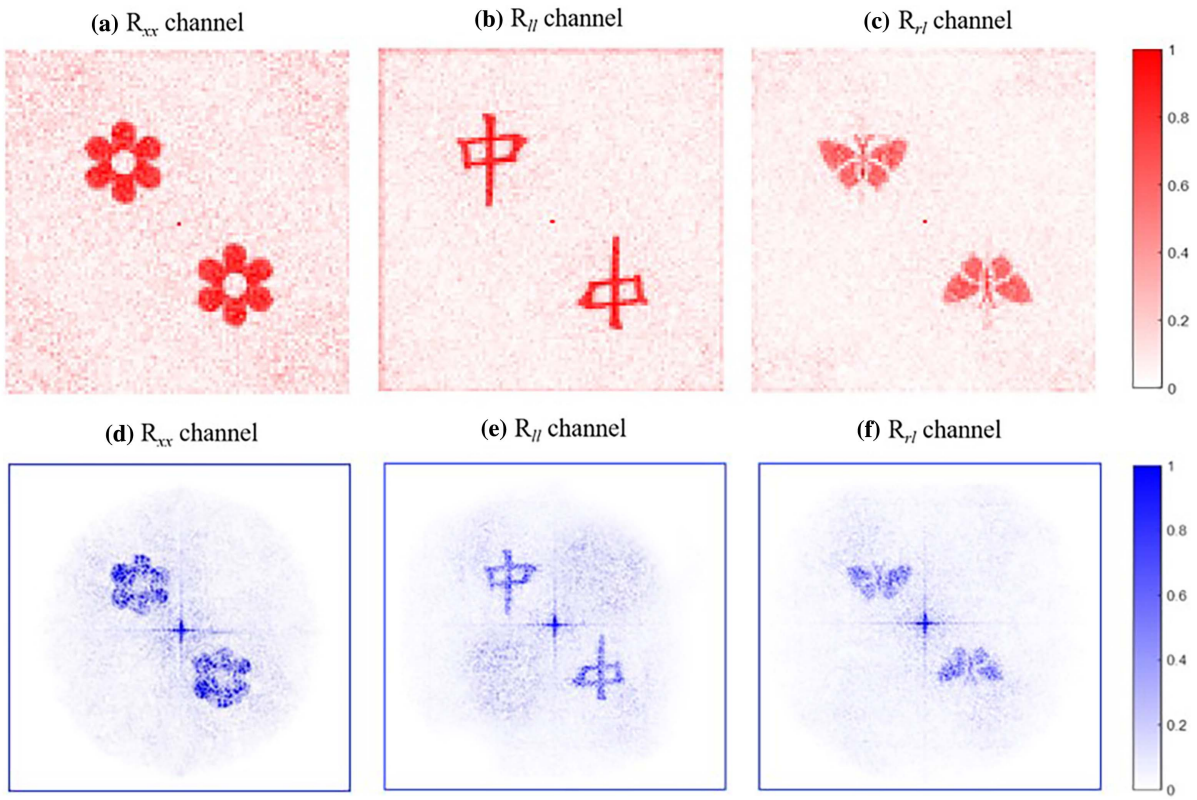

Fig. 7. The multiple reconstructed holographic images within one identical MO metasurface in the different polarization channels. (a)–(c) Numerical reconstructions calculated by the modified GS algorithm. (d)–(f) Simulated reconstructions using full-wave calculations based on FDTD.

magnetize the MO film. The minimum magnetic field intensity used to produce the MO effect is 150 mT, which is the saturation magnetic field intensity of the Bi:YIG, and the objective lens collects the reflective light from the sample and reconstructs the holographic images in the Fourier plane. The reconstructed holographic images are captured by a CCD camera.

5. Conclusion

In summary, we have demonstrated the polarization multiplexing holography of MO metasurface via magnetic control based on the binary amplitude-only hologram. The involved MO metasurface is a tri-layer structure deposited on a glass substrate. Specifically, the rectangular Au nanoantennas are properly arranged on the MO intermediate layer, which is placed on the TiN reflecting layer. We acquire the complex amplitude modulation of the MO metasurface, which changes with the geometric size of the nanoantennas, by using the FDTD method. We deliberately design the nanoantenna arrangement to achieve three independent binary amplitude-only holograms that carry different information in the E_{xx}, E_{ll}, and E_{rl} polarization channels. Three-bits binary amplitude hologram encoding is performed by properly arranging the selected eight nanoantenna structures, which can satisfy all the possible amplitude combinations to incorporate the three holograms into one identical MO metasurface. The holographic images are reconstructed using both the modified binary amplitude GS algorithm and full-wave simulations. The reconstructed holographic images of the MO metasurface switchable in the E_{xx}, E_{ll}, and E_{rl} polarization channels via magnetic control are comparable with the ones based on the GS algorithm, which manifests the dynamic multichannel holographic display function of the MO metasurface. Our proposed MO metasurface holographic multiplexing offers a new paradigm for designing multifunctional metadevices utilizing the MO phenomenon, especially in the optical regime.

Acknowledgements

This work was supported by the National Key R&D Program of China (Nos. 2021YFB2801803 and 2021YFA1401200), the Natural Science Foundation of Shandong Province (No. ZR2023LZH001), the Beijing Outstanding Young Scientist Program (No. BJJWZYJH01201910007022), the National Natural Science Foundation of China (Nos. U21A20140 and 92050117), the Fok Ying-Tong Education Foundation of China (No. 161009), and the Beijing Municipal Science & Technology Commission, Administrative Commission of Zhongguancun Science Park (No. Z211100004821009).

References

1. T. Wang, J. He, J. Guo, *et al.*, "Thermally switchable terahertz wavefront metasurface modulators based on the insulator-to-metal transition of vanadium dioxide," Opt. Express **27**, 20347 (2019).
2. T. Badloe, I. Kim, Y. Kim, *et al.*, "Electrically tunable bifocal metalens with diffraction-limited focusing and imaging at visible wavelengths," Adv. Sci. **8**, 2102646 (2021).
3. S. Li, X. Xu, R. M. Veetil, *et al.*, "Phase-only transmissive spatial light modulator based on tunable dielectric metasurface," Science **364**, 1087 (2019).
4. L. Cong, Y. K. Srivastava, H. Zhang, *et al.*, "All-optical active THz metasurfaces for ultrafast polarization switching and dynamic beam splitting," Light Sci. Appl. **7**, 28 (2018).
5. L. Mao, Y. Li, G. Li, *et al.*, "Reversible switching of electromagnetically induced transparency in phase change metasurfaces," Adv. Photonics **2**, 056004 (2020).
6. X. Zhao, Y. Jiao, J. Liang, *et al.*, "Multifield-controlled Terahertz hybrid metasurface for switches and logic operations," Nanomaterials **12**, 3765 (2022).
7. H. Zhou, Y. Wang, X. Li, *et al.*, "Switchable active phase modulation and holography encryption based on hybrid metasurfaces," Nanophotonics **9**, 905 (2020).
8. J. Sung, G. Lee, and B. Lee, "Progresses in the practical metasurface for holography and lens," Nanophotonics **8**, 1701 (2019).
9. X. Liu, Q. Wang, X. Zhang, *et al.*, "Thermally dependent dynamic metaholography using a vanadium dioxide integrated metasurface," Adv. Opt. Mater. **7**, 1900175 (2019).
10. R. Yang, F. Zhang, Z. Li, *et al.*, "Controllable electromagnetically induced transparency in an electrically tunable terahertz hybrid metasurface," Opt. Laser Technol. **163**, 109380 (2023).
11. M. Ren, W. Wu, W. Cai, *et al.*, "Reconfigurable metasurfaces that enable light polarization control by light," Light Sci. Appl. **6**, e16254 (2017).
12. A. Nagpal, M. Zhou, O. Ilic, *et al.*, "Thermal metasurface with tunable narrowband absorption from a hybrid graphene/silicon photonic crystal resonance," Opt. Express **31**, 11227 (2023).
13. Z. Wang, D. Liao, T. Zhang, *et al.*, "Metasurface-based focus-tunable mirror," Opt. Express **27**, 30332 (2019).
14. Y. Lu, C. Wang, S. Zhao, *et al.*, "Magnetically tunable graphene-based terahertz metasurface," Front Phys. **8**, 622839 (2021).
15. S. Kharratian, H. Urey, and M. C. Onbasli, "Broadband enhancement of Faraday effect using magnetoplasmonic metasurfaces," Plasmonics **16**, 521 (2021).
16. A. Christofi, Y. Kawaguchi, A. Alù, *et al.*, "Giant enhancement of Faraday rotation due to electromagnetically induced transparency in all-dielectric magneto-optical metasurfaces," Opt. Lett. **43**, 1838 (2018).
17. A. I. Musorin, M. G. Barsukova, A. S. Shorokhov, *et al.*, "Manipulating the light intensity by magnetophotonic metasurfaces," J. Magn. Magn. Mater. **459**, 165 (2018).
18. Q. Mu, F. Fan, Y. Ji, *et al.*, "Enhanced terahertz magneto-optical Kerr rotation based on metasurface structure," Opt. Commun. **460**, 125163 (2020).
19. J. Chen, G. Wu, P. Gu, *et al.*, "Theoretical study on metasurfaces for transverse magneto-optical Kerr effect enhancement of ultra-thin magnetic dielectric films," Nanomaterials **11**, 2825 (2021).
20. A. H. Kazemi, A. Mokhtari, and M. Zamaninr, "Graphene-based magneto-optical THz modulator with 100% depth of modulation for communication purposes," Opt. Mater. **123**, 111944 (2022).
21. T. Li, F. Fan, Y. Ji, *et al.*, "Terahertz tunable filter and modulator based on magneto plasmon in transverse magnetized InSb," Opt. Lett. **45**, 1 (2020).
22. N. Dostart, H. Gevorgyan, D. Onural, *et al.*, "Optical isolation using microring modulators," Opt. Lett. **46**, 460 (2021).
23. Q. Mu, F. Fan, S. Chen, *et al.*, "Tunable magneto-optical polarization device for terahertz waves based on InSb and its plasmonic structure," Photonics Res. **7**, 325 (2019).
24. J. Liang, Y. Li, T. Dai, *et al.*, "On-chip Ce:YIG/Si Mach–Zehnder optical isolator with low power consumption," Opt. Express **31**, 8375 (2023).
25. J. Qin, L. Deng, T. Kang, *et al.*, "Switching the optical chirality in magneto-plasmonic metasurfaces using applied magnetic fields," ACS Nano **14**, 2808 (2020).
26. F. Fan, D. Zhao, Z. Tan, *et al.*, "Magnetically induced terahertz birefringence and chirality manipulation in transverse-magnetized metasurface," Adv. Opt. Mater. **9**, 2101097 (2021).
27. L. Li, X. Zong, and Y. Liu, "All-metallic metasurfaces towards high-performance magneto-plasmonic sensing devices," Photonics Res. **8**, 1742 (2020).
28. H. Lu, C. Liu, J. Qin, *et al.*, "Enhanced magneto-optical Kerr effect and index sensitivity in Au/Fe_xCo_{1-x} magnetoplasmonic transducers," Photonics Res. **5**, 385 (2017).
29. J. Qin, S. Xia, W. Yang, *et al.*, "Nanophotonic devices based on magneto-optical materials: recent developments and applications," Nanophotonics **11**, 2639 (2022).
30. A. G. Ardakani, S. Kamkar, and O. Daneshmandi, "Using the circular dichroism of a non-chiral metasurface to detect the magnetic fields," J. Magn. Magn. Mater. **553**, 169263 (2022).
31. S. Chen, F. Fan, X. He, *et al.*, "Multifunctional magneto-metasurface for terahertz one-way transmission and magnetic field sensing," Appl. Opt. **54**, 9177 (2015).
32. S. Yajima, N. Nishiyama, and Y. Shoji, "High-speed modulation in a waveguide magneto-optical switch with impedance-matching electrode," Opt. Express **31**, 16243 (2023).
33. T. Murai, Y. Shoji, N. Nishiyama, *et al.*, "Nonvolatile magneto-optical switches integrated with a magnet stripe array," Opt. Express **28**, 31675 (2020).
34. M. G. Barsukova, A. I. Musorin, A. S. Shorokhov, *et al.*, "Enhanced magneto-optical effects in hybrid Ni-Si metasurfaces," APL Photonics **4**, 016102 (2019).
35. A. Christofi, Y. Kawaguchi, A. Alù, *et al.*, "Giant enhancement of Faraday rotation due to electromagnetically induced transparency in all-dielectric magneto-optical metasurfaces," Opt. Lett. **43**, 1838 (2018).
36. S. Xia, D. O. Ignatyeva, Q. Liu, *et al.*, "Enhancement of the Faraday effect and magneto-optical figure of merit in all-dielectric metasurfaces," ACS Photonics **9**, 1240 (2022).
37. B. F. Díaz-Valencia, E. Moncada-Villa, F. R. Gómez, *et al.*, "Bulk plasmon polariton modes in hyperbolic metamaterials for giant enhancement of the transverse magneto-optical Kerr effect," Molecules **27**, 5312 (2022).
38. E. Moncada-Villa, O. N. Oliveira, and J. R. Mejía-Salazar, "Uniaxial ϵ-near-zero metamaterials for giant enhancement of the transverse magneto-optical Kerr effect," Phys. Rev. B **102**, 165304 (2020).
39. D. Zhao, Z. Tan, H. Zhao, *et al.*, "Active terahertz beam deflection and nonreciprocal spin chirality selection based on magneto-optical P-B metasurface with stacked-graphene layers," Opt. Lett. **47**, 818 (2022).
40. Z. Tan, F. Fan, T. Li, *et al.*, "Magnetically active terahertz wavefront control and superchiral field in a magneto-optical Pancharatnam-Berry metasurface," Opt. Express **29**, 2037 (2021).
41. Y. Bi, L. Huang, R. Zhao, *et al.*, "Magnetically controllable holographic encryption based on a magneto-optical metasurface," Opt. Express **30**, 8366 (2022).
42. C. Lei, L. Chen, Z. Tang, *et al.*, "Enhancement of magneto-optical Faraday effects and extraordinary optical transmission in a tri-layer structure with rectangular annular arrays," Opt. Lett. **41**, 729 (2016).
43. V. I. Belotelov, L. L. Doskolovich, and A. K. Zvezdin, "Extraordinary magneto-optical effects and transmission through metal-dielectric plasmonic systems," Phys. Rev. Lett. **98**, 077401 (2007).
44. D. W. Lynch and W. R. Hunter, *Handbook of Optical Constants of Solids* (Academic, 1985).